Charles University in Prague
Faculty of Mathematics and Physics

MASTER THESIS

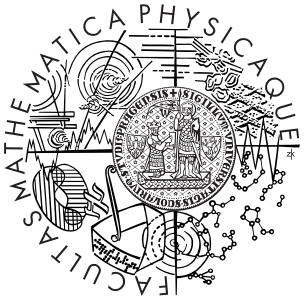

Tomáš Javůrek

Tile calorimeter response to muons

(Odezva kalorimetru Tilecal na miony)

Institute of particle and nuclear physics

Supervisor of the master thesis: RNDr. Tomáš Davídek, Ph.D.

Study programme: Physics
Specialization: Nuclear and subnuclear physics

2012

Acknowledgment:

I thank my supervisor RNDr. Tomas Davidek, Ph.D. and co-supervisor Doc. RNDr. Rupert Leitner, DrSc. for their invaluable guidance, the materials they gave me and many useful suggestions during my work. I also thanks to Martina Pagacova for her good ideas and comments to this work. Other thanks goes to Jaroslava Schovancova, Zhili Weng and Lei Zhang for their technical support with data analysis. Special thanks goes to my family and friends for their great support and care.

Prohlašuji, že jsem tuto diplomovou práci vypracoval samostatně a výhradně s použitím citovaných pramenů, literatury a dalších odborných zdrojů.

Beru na vědomí, že se na moji práci vztahují práva a povinnosti vyplývající ze zákona č. 121/2000 Sb., autorského zákona v platném znění, zejména skutečnost, že Univerzita Karlova v Praze má právo na uzavření licenční smlouvy o užití této práce jako školního díla podle §60 odst. 1 autorského zákona.

V Praze dne 10.4.2012 Tomáš Javůrek

Contents

Název práce: Odezva kalorimetru TileCal na miony
Autor: Tomáš Javůrek
Katedra (ústav): Ústav částicové a jaderné fyziky
Vedoucí bakalářské práce: RNDr. Tomáš Davídek, Ph.D.
e-mail vedoucho: davidek@ipnp.troja.mff.cuni.cz

Abstrakt: Cílem této práce je zkoumat odezvu kalorimetru TileCal (subdetektoru na experimentu ATLAS) na miony. Miony mohou v tomto hadronovém detektoru sloužit k odhalení prostorových odchylek. K tomu účelu jsou použity grafy uniformity neboli závislosti dE/dx (deponovaná energie na jednotku dráhy) na azimutalním úhlu ϕ a na polárním úhlu θ, který je reprezentován pseudorapiditou η. Nakonec byla také zkoumána závislost dE/dx na energii mionu.

Klíčová slova: TileCal, mion, uniformita, energetické ztráty

Title: Tile Calorimeter response to muons
Author: Tomas Javurek
Department: Institute of Particle and Nuclear Physics
Supervisor: RNDr. Tomas Davidek, Ph.D.
Supervisors e-mail address: davidek@ipnp.troja.mff.cuni.cz

Abstract: The aim of present work is investigation of Tile calorimeter (subdetector of ATLAS experiment) response to muons. Muons can help to monitor spatial non-linearities in this hadronic detector. Graphs of unifromities are used for these purposes i.e. dependence of dE/dx (deposited energy per unit length) on azimuthal angle ϕ and polar angle θ which is represented by pseudorapidity η. Finally the dependence of dE/dx on energy was also studied.

Keywords: TileCal, muon, uniformity, energy loss

Chapter 1

Introduction

CERN (The European Organization for Nuclear Research) was founded in 1954 as a community unifying european particle physicists after the Second World War. Initially, there were 12 member states but that number has increased by 8 up to now. Czech republic and Slovakia joined the CERN membership in 1993.

During nearly 60 years of the CERN existence, a lot of important discoveries and observations have been done and its indispensability for technical progress is more than obvious. Not only well known LHC (Large Hadron Collider) but there were several accelerators, both colliders and linear accelerators. One can mention SPS (Super Proton Synchrotron) where W and Z bosons were discovered or LEP (Large Electron-Positron Collider) which provided precise measurement of some Standard model quantities, particularly masses of intermediate vector bosons. Most of the accelerators work till today, for example as the preinjectors for LHC or as a source of neutrinos. LEP had to be dismantled to provide the place for LHC.

There are four intersection points on LHC where huge detectors are installed. Largest one is called Atlas (A Toroidal LHC Apparatus).

TileCal, subdetector of Atlas experiment, and its response on muons are studied in this thesis. The electronics, the mechanics and other theoretical principles are introduced in the first part (chapters 4-8). The results of data analysis, interesting plots and conclusions both from the monte carlo and from the collision data are discussed in the second part.

Chapter 2

LHC

The LHC, a 27 km long synchrotron, is designed to produce proton-proton collisions with centre-of-mass energy 14 TeV that makes it the largest and the most energetic accelerator in the world. It was installed in the existing tunnel which had been used for LEP. The first beam was turned on in September 2008 and again after reconstruction break at October 2009. Nowadays, the stable beams are commonly reached and the plan is to increase the luminosity to the designed one (current highest reached luminosity is $3.65 \cdot 10^{33}\mathrm{cm}^{-2}\mathrm{s}^{-1}$ in October 2011).

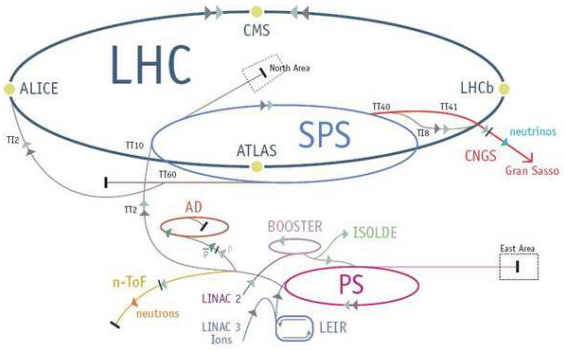

Figure 2.1: LHC and its preinjectors Ref. [1].

The LHC can accelerate both protons and heavy ions by synchronizing the electric and magnetic field with the moving particles. The operation of the beam is managed by the superconducting magnets (toroids). The particles in such a collider can not be accelerated from negligible energy to

the energy of order TeV because of necessary phase transitions. Therefore, there are many preinjectors beginning with Linac which boosts protons to the energy 50 MeV, then PSB (Proton Synchrotron Booster) up to 1.8 GeV, next PS (Proton-Synchrotron) accelerates them to 26 GeV and last step before LHC is SPS (Super Proton Synchrotron) where protons get 450 GeV. The schema of the acceleration is shown in Fig. 2.1.

The production of particles is characterized by the rate R defined as:

$$R = \sigma L \tag{2.1}$$

where L is the luminosity:

$$L = \frac{N^2 f}{4\pi\sigma_x\sigma_y t} \tag{2.2}$$

N - the number of protons per bunch,
f - the frequency of bunch crossing,
t - the time between bunches,
σ_x and σ_y - transverse dimensions of the Gaussian beam profiles

The nominal LHC beam bunch-crossing period is 25 ns and designed luminosity is $10^{34}\text{cm}^{-2}\text{s}^{-1}$. One can expect 23 interactions per crossing. These parameters are sufficient for measuring many diverse processes including statistically suppressed one.

There are four main detectors in the interaction points on LHC: ATLAS, CMS, ALICE and LHCb. The experiments ATLAS and CMS are designed for studying of many diverse processes whereas LHCb and ALICE are specialized in relatively shorter range of interests. The experiment ALICE is focused on studying the quark-gluon plasma created by Pb-Pb collisions. The LHCb focuses on the measurement of CP violation in interactions of B-hadrons. The main purpose of ATLAS and CMS is the exploration of the origin of spontaneous symmetry-breaking namely the origin of the particle masses. Another goals of ATLAS is also CP violation in B decays, precise measurement of top quark and W masses.

There are also two much smaller experiments TOTEM and LHCf. They are designed to study the forward particles in elastic pp scattering and measuring of cross sections in forward processes.

Chapter 3

ATLAS

The ATLAS detector is situated in Point 1, the intersection point closest to the CERN. This huge giant depicted in Fig. 3.1 is installed in the cavern 100 m deep under ground. The detector reaches 45 m in length and 22 m in height and weights about 7000 t. As it is essential to detect all produced particles, ATLAS is composed of several detectors focused on different particles. A brief overview of ATLAS subdetectors is given in this chapter.

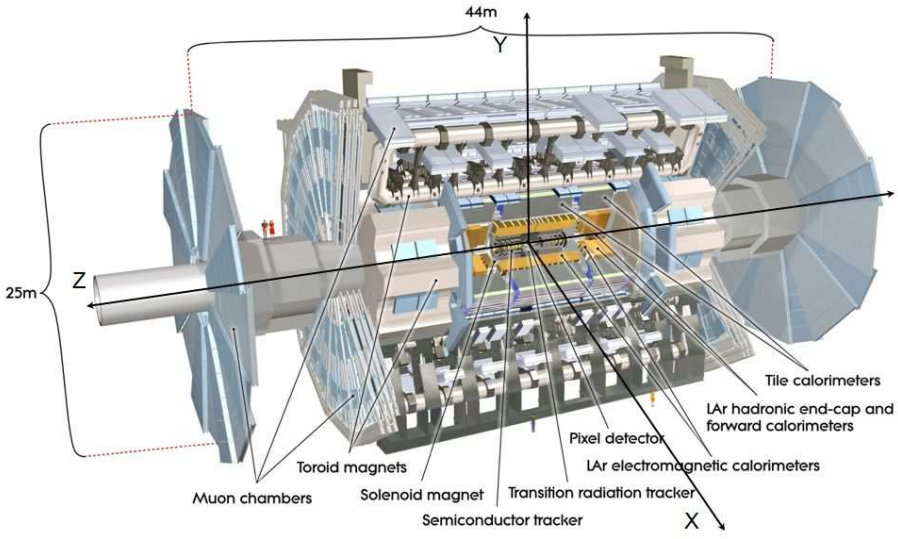

Figure 3.1: ATLAS and its coordinate system Ref. [2].

3.1 Atlas coordinate system

The system of axis definition is depicted in Fig. 3.1. The origin is placed to the interaction point, z axis is defined in the direction of beam, x axis points to the centre of LHC and y axis points upwards. The azimuthal angle ϕ is measured from positive x direction and angle $\pi/2$ is reached in positive y direction. The polar angle θ (in yz plane) goes form 0 to π beginning in z axis, value of polar angle is 0 in direction of z axis to the right on Fig. 3.1.

One usually talks in terms of pseudorapidity defined as:

$$\eta = -\ln\tan(\frac{\theta}{2}) \tag{3.1}$$

Than $\eta = 0$ in xy plane perpendicularly to the beams and $\eta \sim \pm\infty$ in direction close to the beams.

3.2 ATLAS subdetectors

Inner detector

Inner detector is the innermost part of ATLAS detector specialized to measure momentum and position of charged particles with high precision. The outer radius is 115 cm and its length is 7 m. Its coverage in terms of pseudorapidity is $\eta \leq 2.5$. Whole detector is placed into 2T strong solenoid magnetic field that is used to the momentum determination. Inner detector consists of three subsystems: Pixel Detector, Semi-Conductor Tracker (SCT) and Transition Radiation Tracker (TRT).

Pixel Detector and SCT form together the precision tracker designed to provide good spatial resolution. The first one consist of about 80 millions silicon pixels working as diodes driven in a reverse-bias mode. The second one is composed of long silicon strips. The outermost subsystem of Inner detector is TRT. Its base consists of the straw tubes which are filled by xenon so the charged particle lose their energy by radiation. The electron can be then identified by magnitude of transition radiation.

Calorimeter

ATLAS calorimeter is made of two components: LAr (Liquid Argon) and tiles. Its main purpose is to measure energy and direction of jets, electrons,

photons and single hadrons that also help to determine missing transverse energy (E_t) given by neutrinos.

Electromagnetic part of LAr covers the region $|\eta| < 3.2$. There are also two LAr hadronic parts: end-cap calorimeter which covers $1.5 < |\eta| < 3.2$ and forward calorimeter covers even $3.1 < |\eta| < 4.9$. TileCal (Tile Calorimeter) is another hadronic part with coverage $|\eta| < 1.7$. LAr electrodes in shape of accordion collect the charge from ionization of charged particles in active medium (liquid argon). Almost all electrons are absorbed in LAr. Similarly TileCal absorbs most of hadrons. The TileCal is discussed in detail in chapter 4.

Muon spectrometer

From known particles only muons and neutrinos are able to reach muon spectrometer, other are absorbed earlier in detectors closer to the interaction point. Of course neutrinos can't be detected in any subdetector because they are leptons with zero charge.

There are four different technologies used within the Muon Spectrometer that have different spatial and timing resolutions: Monitored Drift Tube chambers (MDT), Cathode Strip Chambers (CSC), Resistive Plate Chambers (RPC) and Thin Gap Chambers (TGC) Ref.a [3]. As muons interacts only by weak force, the detector has to have big volume. Therefore muon chambers has to be last subdetector of any detector like ATLAS. Muon spectrometer is inserted in 2-6 [T.m] non-homogeneous magnetic field to provide the measurement of deflection of muon track thus the muon momentum.

Chapter 4

Tile Calorimeter

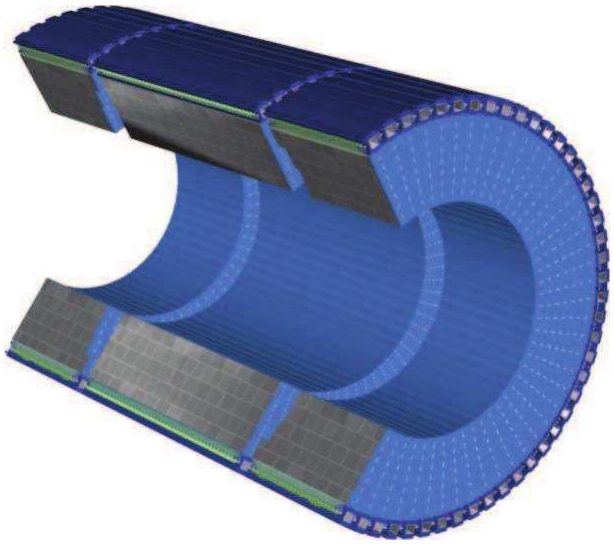

Figure 4.1: TileCal Ref. [4].

4.1 Mechanics

TileCal subdetector is a part of the hadron calorimeter which is situated in the middle of ATLAS detector adjoined to the inner shell of muon spectrometer. TileCal is divided into the left-right external barrels (EB) in pseudorapidity range $0.8 < |\eta| < 1.7$ and middle long barrel (LB) in pseudorapidity range $|\eta| < 1.0$ separated by gaps (Fig. 4.1 and Fig. 4.2). Outer

and inner radius of TileCal are 4230 mm and 2280 mm respectively. TileCal is a little asymmetric in η that is usually not mentioned in papers. While the back edge of EB is 6113 mm far in positive z direction ($\eta > 0$), the back edge of EB in negative z direction is 6103 mm far from origin of coordinate. In fact whole left EB is shifted by 10 mm compared to the right EB. All proportions and positions of the TileCal cells are introduced in appendix A.

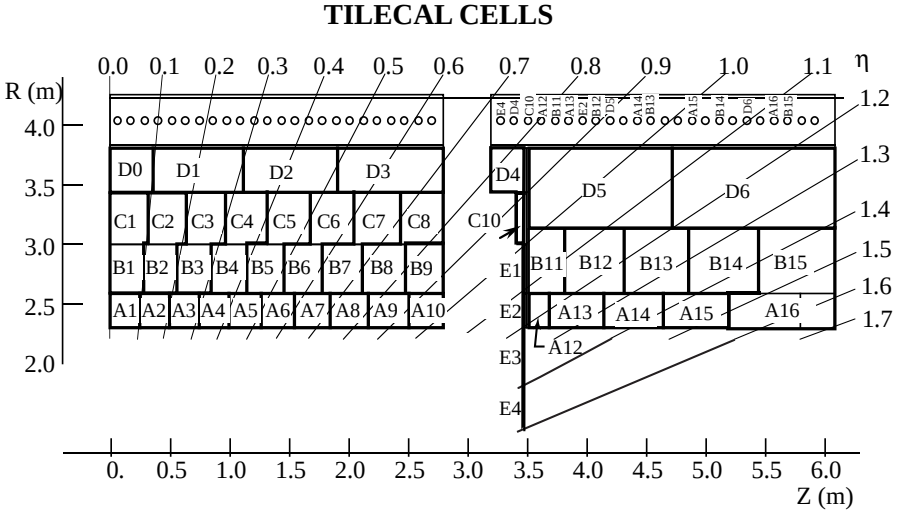

Figure 4.2: Cell geometry Ref. [5].

Both EB and LB barrels consist of 64 modules in ϕ direction meaning that one module spans $\triangle\phi \sim 2\pi/64 = 0.1$. Each module is composed of three radial layers assigned as layer A, layer BC, layer D. These layers are divided into cells from the read-out point of view. Moreover, there is a special part of EB called ITC (Intermediate Tile Calorimeter). One can see on Fig. 4.2, that these cells are located in gap between EB and LB. So called gap scintillators E1, E2 and crack scintillators E3, E4, consists only from active medium. Other ITC cells C10 and D4 have normal periodic structure[1].

The Tile Calorimeter main task is to measure the energy deposit with a dynamic range from ∼200 MeV/cell for muons or MIP to TeV/cell for jets. For these purposes, the steel is chosen as passive component of detector which is periodically alternated with scintillating polyethylene tiles Fig. 4.3.

[1]scintillators alternate with passive medium, see next paragraph

One 18 mm thin period is made of 3 mm tile, 14 mm passive medium and 1 mm gap. These plates are placed perpendicularly to the beam z axis. The proportions of such plate in horizontal direction vary between 200-400 mm depending on the r position of the plate. Azimuthal ϕ dimensions varies between 100-200 mm dependently on the position of the cell where the plate is placed. In whole TileCal there is 460 000 tiles and 640 000 WLS (Wave Length Shifting) fibres transporting signal to the photomultiplier. Thin space between modules is designated for these fibres. Front-end electronics is coupled into superdrawers installed inside a steel support called grider which is fixed at the top of module.

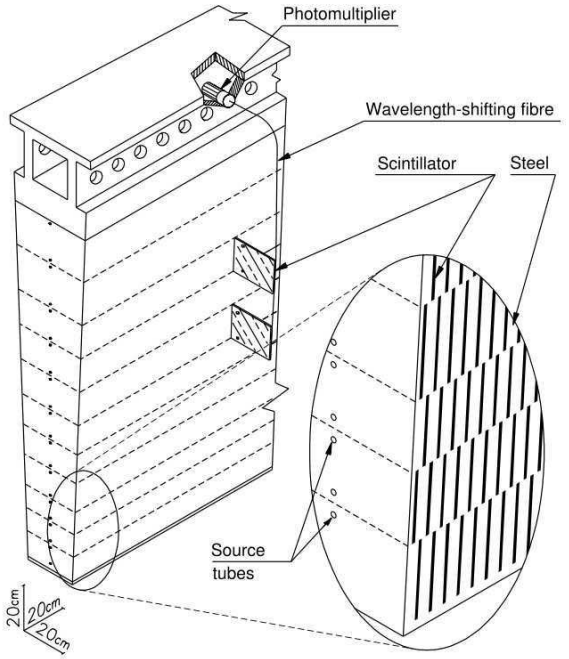

Figure 4.3: TileCal module Ref. [2].

4.2 Optics and electronics

The electronics is divided into the front-end electronics which is placed in superdrawers and the back-end electronics which is located outside of the TileCal. A brief story of signal going from TileCal cells through front-end electronics to the back-end electronics is described in this chapter.

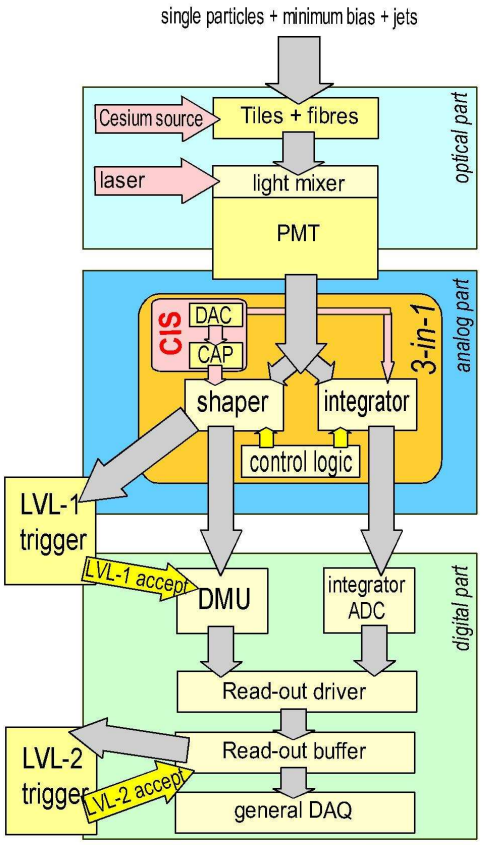

Figure 4.4: Schema of front-end electronics Ref.[8].

Schema of the main parts optics and read-out electronics is depicted in Fig. 4.4. First step is the scintillating tile where UV light is emitted by deexciting polyethylene molecules. Thin scintillating tile is shown in Fig. 4.5.

Photons from scintillators are conducted by WLS fibres to PMT (Photomultiplier). This UV light has to be shifted by WLS fibres to provide optimal condition for emission of primary electron from photocathode. Between fibres and PMT, there is light mixer which is responsible for minimization of the response dependence on position of the fibres on surface of the photocathode which receives the light. Light mixer, PMT, Divider and 3-in-1 card are partitions of so called PMT block. Next stage after light mixer is the PMT which converts light signal to electric charge. HV divider distributes high voltage to PMT dynodes and also plays a role of socket between PMT

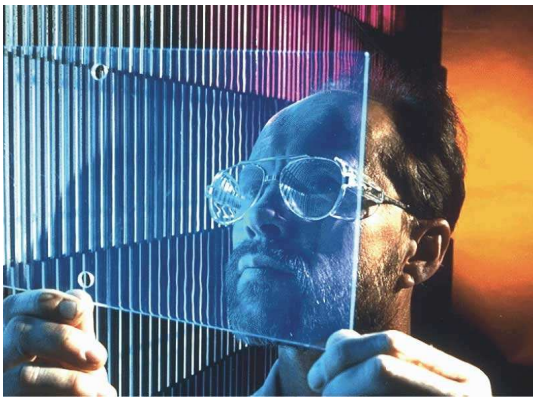

Figure 4.5: Picture of scintillating tile Ref.[16].

and the rest of front-end electronics. This compression without interconnection wires minimises the resistance and noise. Last stage of PMT block is 3-in-1 card which has these three main outputs:

- fast signal to LVL1 trigger
- LG (low gain) and HG (high gain) signals to digitizer
- output for MB (minimum bias) and Cs calibration (Chapter. 4.3)

The 3-in-1 card consists of two partitions: shaper and integrator. The integrator measures current from MB interactions and Cs radioactive source. It is averaged over longer time and used for monitoring and calibration of a single cell. The shaper transforms (amplifies and spreads) the analog signal from PMT with about 18 ns FWHM to the signal with approximately 50 ns FWHM and sends it to the digitizer. There are two types of distributed signal: HG (high gain) and LG (low gain). HG is 64x amplified compared to LG and is used for particles with low energy deposit typically less than 12.5 GeV.

Analog signal from shaper continues to digitizer board Fig. 4.6 which contains twelve 10-bit ADC (analog to digital converter) and two TileDMU chips. Its main role is to convert the pulse from analog signal to digital one. TileDMU receives TTC signal (The ATLAS Timing, Trigger and Control) from TTCrx chip and sends a command for the readout to the ADC. It means that pulse is sampled (usually 7 times with interval 25 ns) in ADC by this TTC signal. TTC signal is synchronized with bunch crossing and

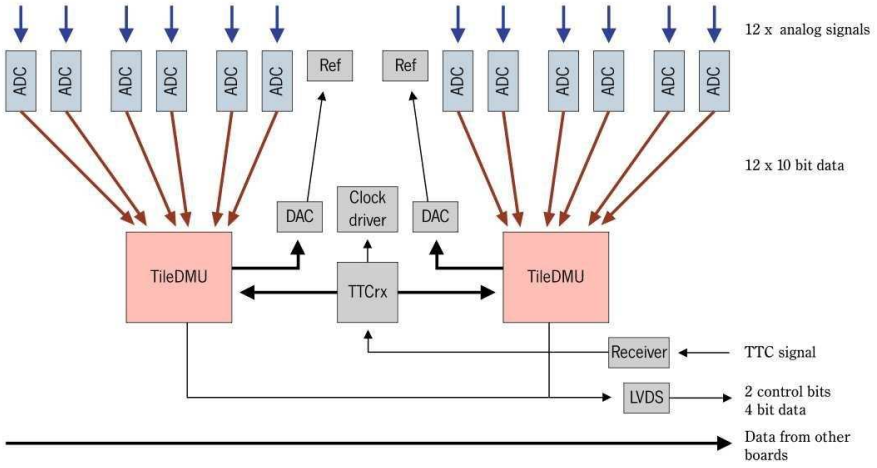

Figure 4.6: Digitizer board. Twelve ADC are linked to two TileDMU Ref. [7].

appropriate delay is given by TTCrx. TileDMU is also responsible for reformatting and reordering of the digitized data. The digitized data is stored to the pipeline memory which can hold about 1000 digits. It gives LVL1 2.5 μs to make a decision whether data is accepted or not. Data is sent to the back-end electronics through interface links in case of positive LVL1 trigger decision or removed in opposite case.

The scheme of back-end electronics is depicted in Fig. 4.7. The principal point of the back-end electronics are RODs (Read-Out Drivers). RODs are responsible for data gathering after LVL1 trigger decision and data processing. Amplitude, quality factor and time delay of signal after bunch crossing are reconstructed using OF method (optimal filtering) Ref. [10] and also calibration constants are applied. Such data is sent to the LVL2 trigger and to the ROBs (read-out buffers) where they are stored for LVL2 trigger decision and for next data processing. ROD can also stop LVL1 trigger generation if busy.

4.3 Calibration and monitoring

In order to assure a high quality performance of TileCal detector, it is necessary to manage calibration and monitoring during the data taking. The

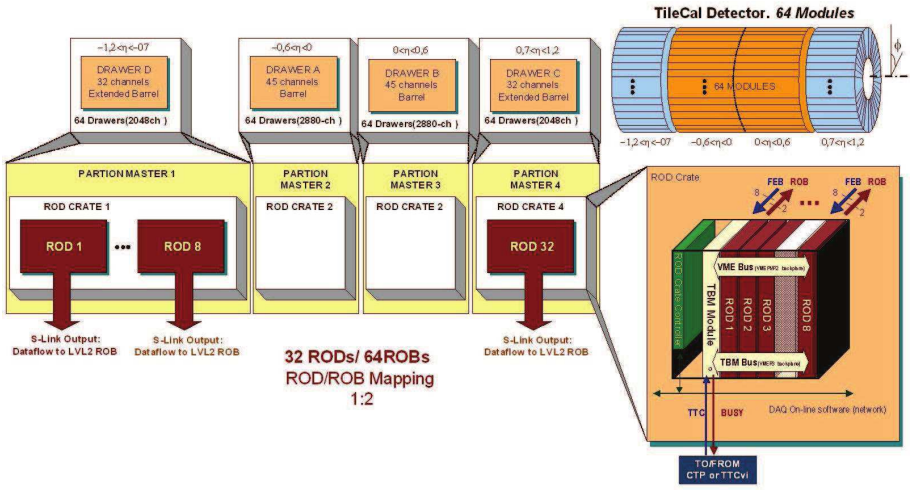

Figure 4.7: Schema of Back-end electronics. There is 32 read-out drivers: 8 for each barrel Ref. [9].

energy and timing have to be determined with good precision. Roughly said there are two attitudes which has to be managed:

- to measure calibration factors of each read-out channel (output of PMT)
- to analyze these factors over long time in order to monitor whole detector in time and calibrate measured quantities

Calibration factors appears in equation for measured energy in one channel $E_{channel}$ knowing the amplitude A measured in ADC counts:

$$E_{channel}[\text{GeV}] = A[\text{ADC}] \cdot C_{CIS} \cdot C_{laser} \cdot C_{Cs} \cdot C_{TB}[\text{GeV/pC}] \qquad (4.1)$$

Subscripts of factors C_{CIS}, C_{laser} and C_{Cs} corresponds to calibration systems discussed in the following text. Factor C_{TB} corresponds to the electromagnetic scale. Its value 1.050±0.003 [GeV/pC] was set at test beam 2001-2003 Ref. [17].

TileCal calibration systems are differ by the time of determining calibration factors and each of them monitors definite part of downstream electronics, as it is shown on Fig. 4.8. Brief description of four main calibration

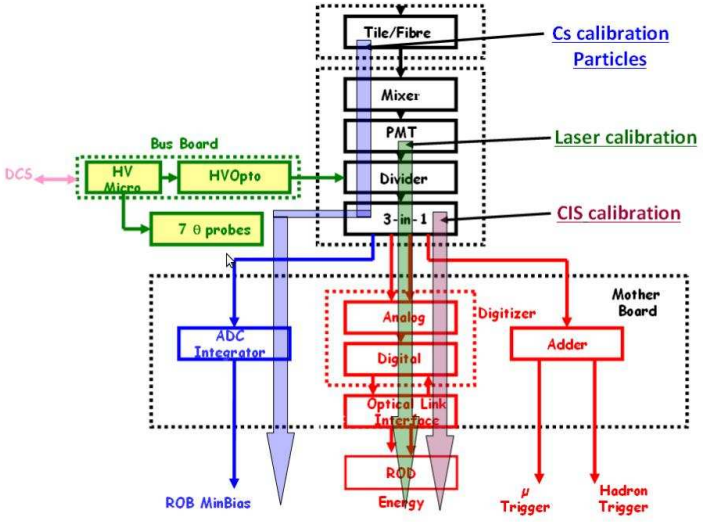

Figure 4.8: Schema of calibration systems and their position in downstream electronics Ref. [11].

methods is given in this chapter, more detailed description can be found in Ref. [13].

The Cs calibration system

The 137Cs source propelled by water can be pumped into the system of copper pipes which go through each tile of TileCal. Small holes on edges of each tile or absorber determined for Cs pipes are shown on Fig. 4.3. This system was used to set the initial gains of all PMTs but now it is used occasionally to monitor response of individual cells. It takes about 5 hours to do a calibration run over all TileCal cells. It is obvious, that it can not be done during physics run unlike next calibration methods.

The Laser System

The laser system is designed to calibrate and monitor the response of the PMTs with an accuracy better than 0.5%, both during ATLAS data collection and in special calibration runs. The principle of operation of the laser system is to inject a common light signal (532 nm) to all PMTs that will produce a response similar to the one produced by the ionizing particles in

the scintillating tiles. This method helps to monitor the PMT stability and linearity and but can be also used to study pulse saturation. Injection of light has to be synchronized with bunch-crossing clock in order to process when there are no signals from real particles and also for trigger recognition of calibration signals.

The Charge injection system (CIS)

Well defined charge signal with a systematic uncertainty is injected to the front-end electronics in order to reproduce the photomultiplier output. It is used to produce calibration factor of conversion ADC counts to charge both gains LG and HG. This factor is calculated for each channel with accuracy 0.7%. The CIS calibration processes in periodic runs during beam-off period.

Minimum bias monitoring system (MB)

If the inelastic pp collision with low momentum transfer happens, the MB (minimum bias) particles can be produced. The rate and consequently energy depositions of MB particles does not depend on ϕ and temperately on η but is proportional to LHC luminosity. One can expect in average 23 MB events/bunch crossing at designed LHC luminosity $10^{-34}\mathrm{cm}^{-2}\mathrm{s}^{-1}$ i.e. it takes few milliseconds to have constant mean current on PMT anode.[1]

[1]Disadvantage of this online method is that MB particles usually don't penetrate through whole TileCal. Muons can be used in case of offline studies of spatial non-linearities. Moreover, unlike the MB particles, muons usually pass through whole calorimeter.

Chapter 5

Trigger, data acquisition and data collection

Considering that the bunch crossing rate is 40MHz and offline computing is limited to 200Hz, an effective data selection of attractive processes is needed. Therefore three trigger systems LVL1, LVL2 and EF (Event Filter) adjudicate on event acceptance during the signal flow through TileCal electronics. Specific selection criteria are applied on each trigger level to keep the trigger rates constant, independently on the luminosity changes. Trigger positions in TileCal are depicted on Fig. 4.4.

The LVL1 trigger operates with simple but efficient algorithms to determine quickly the interesting physics. It receives information from Muon Spectrometer and calorimeters and determine particles using local pattern recognition and transverse energy. It takes approximately 2μs. Data has to be kept in a pipeline memories during this intermission. Output rate of LVL1 is 100 KHz meaning that LVL1 reduces event rate by factor 103. Data is also sent to the RODs for further calibrations or tests.

The LVL2 trigger uses RoI (Regions of Interest, see Fig. 5.1) provided by LVL1 trigger to refine the selection of candidate of objects. It uses full-granularity information from all detectors, even from the inner detector which is not used at LVL1. Therefore it takes 10ms to make a decision by LVL2 while data is sored in ROBs. Event rate is reduced to 2KHz by LVL2.

Last level in triggering chain is EF (Event Filter). Information about the event is stored in many ROBs. These fragments are collected to the full-event data by Event Builder and next physical selection criteria are applied by EF. It takes 4 sec. to process and event rate is reduced to 200 Hz. More

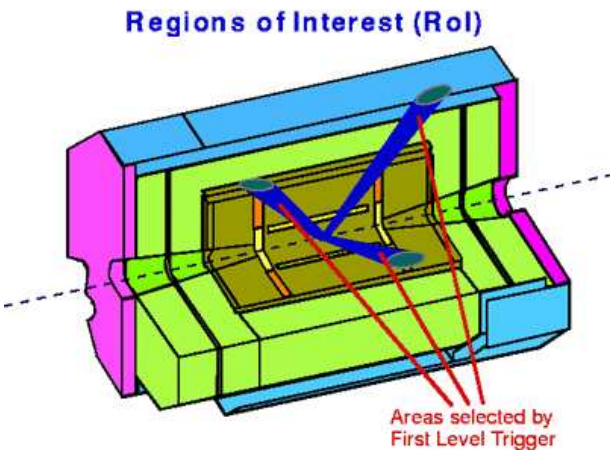

Figure 5.1: Regions of Interests [16]

detailed description can be found in Ref. [16].

As ATLAS produces big amount of data, lot of devices for storing and distributing data is needed. For these purposes the system of Tier facilities is built as it is shown on Fig. 5.2 . Raw data from EF are distributed to Tier-0 facility at CERN where they are sored approximately for 5 days waiting for the first failure notices. Since RAW data has 1.6 MB for single event, it is too large to handle it for long time. Therefore kind of derived data are produced and distributed to higher degrees. Basically, there are two types of data produced by Tier-0: ESD (Event Summary data, 0.5 MB) and AOD (Analysis Object data, 100 kB). These types of data are then sent to the higher Tier sites, where they are available for analysis[1]. More detailed information about data acquisition can be found in Ref. [19].

[1]It is possible to analyze data in AOD or ESD format using athena (environment for python programing) or can be convert to ntuples which are more comfortable to work with using Root Ref. [14]. In this thesis, we used TileMuonDumper produced by Zhili Weng and Lei Zhang to compress data of both format AOD and ESD to ntuples.

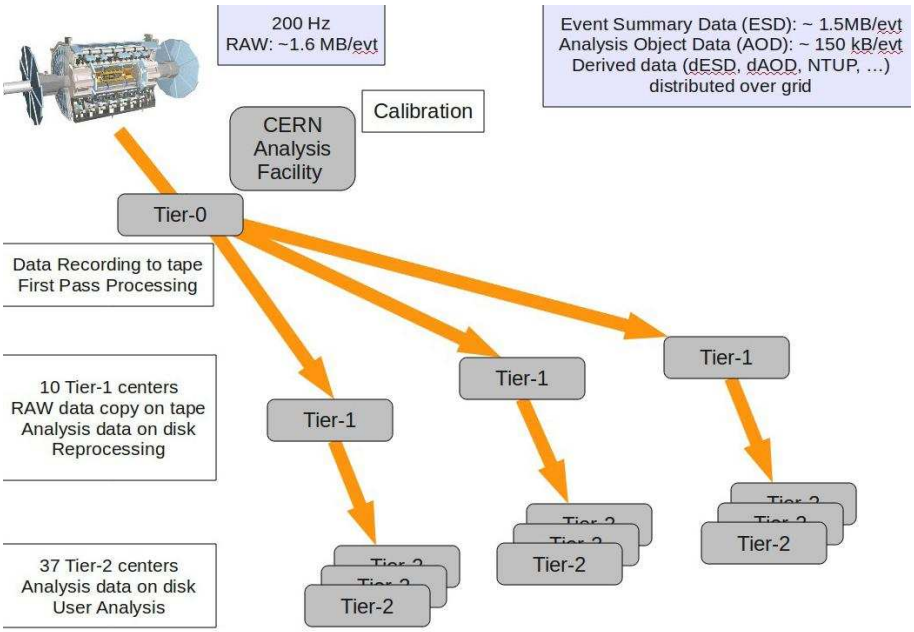

Figure 5.2: Data collection, the system of Tier facilities Ref. [15].

Chapter 6

Physics Motivations

As it have been mentioned in previous chapters, muons have clean signature in calorimeters and therefore can by used as tool for monitoring TileCal. Moreover there are no competitive particles that pass through whole calorimeter with non-negligible energy loss.

Another motivation for studying muons in calorimeters is that additional information for muon reconstruction can be produced. Muon spectrometer and inner detector are used for primary reconstruction but response from TileCal can improve the energy precision. This can help to improve analysis of processes where muons are produced. For completeness of physical motivations some of such processes are introduced:

1)$Z \to \mu\mu$, $\Upsilon \to \mu\mu$, $J/\psi \to \mu\mu$ ...
2)$H \to WW \to \mu\nu_\mu l\nu_l$, $H \to ZZ \to \mu\mu ll$ (H stands for SM Higgs boson, l stands for lepton that can be also muon)[1]
3) processes with intermedial vector bosons or virtual photon, for instance Drell-Yan.

[1]At the present time, when these thesis are written, still is not known whether Higgs particle exists or not.

Chapter 7

Muons in calorimeter

Muons interact with matter by several ways dependently on the muon energy Ref. [12]. The main processes for high energy muons are ionization and radiative losses. "Radiative" means some kind of photon emission on Feynman diagram level. One can divide radiative losses into: pair production (emission of (virtual) photon which splits into e^+e^- pair), bremsstrahlung (photon production caused by deceleration of muon) and photonuclear interaction (interaction of photon with nuclei).

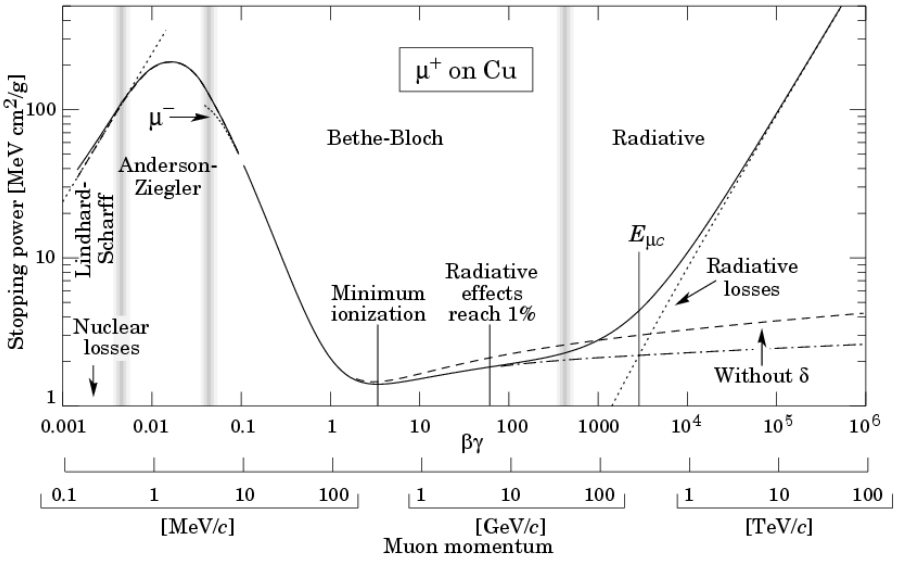

Figure 7.1: Muon energy loss in Cu Ref. [6].

In this thesis, there is also studied range of muon energy 10-100GeV. An acceptable approximation for such muons is derived from Bethe-Bloch Eq. (7.1) which describes the ionization looses in the middle region of energies shown in Fig. 7.1.

$$\frac{dE}{dx} = C_1 \left(\frac{1}{2} \frac{C_2 E^4}{1 + 2\frac{m_e}{m_\mu}\frac{E}{m_\mu} + \frac{m_e^2}{m_\mu^2}} - \frac{3}{2} - ln\frac{E}{m_\mu} - ln\frac{\hbar\omega}{I_e} \right) \tag{7.1}$$

where constant C_1 (roughly values in bracket are meant for TileCal):

$$C_1 = \frac{4\pi e^4 \rho N_a Z}{A m_e c^2} \quad (= 0.856 \text{ MeV/cm}) \tag{7.2}$$

Z resp. A is proton resp. nucleon numbers of absorber and ρ density of absorber. The constant C_2 in Eq. (7.1) can be expressed as:

$$C_2 = \frac{4me^2}{I_e^2 m_\mu^4 c^4} \quad (= 0.1027 \text{ MeV}^{-4}) \tag{7.3}$$

I_e stands for mean excitation energy. Last term in Eq. (7.1) include plasma energy $\hbar\omega$ and its approximate value is $ln\frac{\hbar\omega}{I_e} = 7.3$.

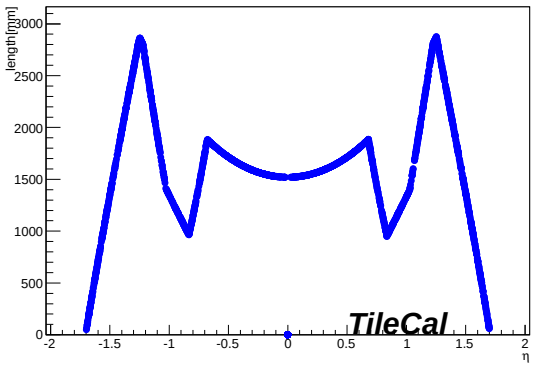

Figure 7.2: Muon track length in TileCal, dependence on direction: $|\eta| < 1.7$, peaks are the longest path in TileCal in direction of back up edge of D6 cell, short path length ∼1 m in $|\eta| \sim 0.7$ is caused by gap between EB and LB.

As the average length of the muon passage through the TileCal is 2m (see. Fig. 7.2, similar plot can be found in Ref. [8]), the energy loss in whole

TileCal for one 50 GeV muon is approximately 3 GeV which is very low in comparison with hadrons or jets.

Ionization loss (described by Bethe-Bloch Eq. (7.1)) is dominant for low energies. Radiative contribution begin to play important role in intermediate range of energies ($\sim$ 100GeV). Critical energy $E_{\mu c}$ is defined as energy when radiative losses are equal to ionization, for muon in iron it is 347 GeV. Total contribution for such energies is parameterized as:

$$-\frac{dE}{dl} = a(E) + b(E)E \tag{7.4}$$

where term $a(E)$ stands for ionization contribution and $b(E)E$ for radiative losses. Parameter $b(E)$ can be considered constant for high muon energy approximately TeV.

One can expect that the response of TileCal on muons per unit length should be the same for all directions i.e. independent on η and ϕ. This feature is called uniformity and the graphs of uniformity (dependence of response measured in MeV/cm on η, ϕ) give us a tool for monitoring TileCal. As was mentioned above muons are measured with bad accuracy and a lot of events is needed. Than the graph of uniformity is filled by mean or truncated mean values of muons energy loss.

Distribution of the muon energy deposit in definite direction with definite momentum is provided by the convoluted Landau and Gaussian[1] function, which could be used for fitting in case of sufficient statistics.

[1]Energy losses themselves are given by pure Landau distribution, Gaussian contribution is given by TileCal energy resolution.

Chapter 8

Muon reconstruction and identification

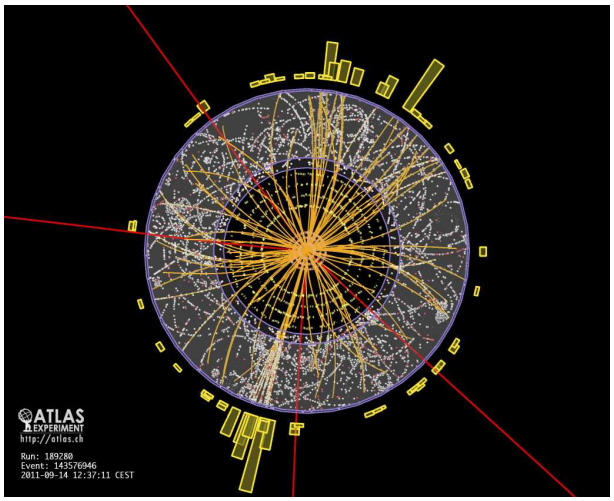

Figure 8.1: Event in Inner detector Ref. [20].

As the energy of pp collisions increases, a huge amount of particles can appear mainly in Inner detector leading to the abundant response in whole detector. It is not easy to choose the trajectory of particle from such 3D map of hits and determine its momentum (Fig. 8.1). Therefore sophisticated but fast tool for track reconstruction is needed. There are two tracking systems, the Inner Detector and the Muon Spectrometer, that provide precise measurements of the momentum, charge and direction of motion. Several al-

gorithms are used for the tracking purposes, such as pattern recognition and track fitting. Quite nice explanation of this topic can be found in Ref. [22].

Pattern recognition is the method that selects hits belonging to the same trajectory. It is based on Hough transformation which converts well defined trajectory passing through some hit to the point in Hough space. Many trajectories passing through given hit form the function. Hough space is the set (it is done for all hits) of such functions whose parameters are perigee (distance of trajectory from origin) and direction of trajectory in the point of hit. In case of straight line trajectory in 2D, it is:

$$x \sin \phi - y \cos \phi = R_0 \tag{8.1}$$

x, y ... coordinates of hit
ϕ ... angle between x and trajectory
R_0 ... perigee

The point in Hough space where is an intersection of more functions represents the trajectory candidate via Hough transformation. Intersection in Hough space is found by binning and histogramming.

Track fitting gives the best estimate of the parameters taking the initial parameters information from pattern recognition. There are basically two types of track: fitters the Kalman Fitter Ref. [23] and the GlobalChi2Fitter Ref. [24]. Kalman Fitter is based on Kalman filter which recursively precises the mean and the variance. The GlobalChi2Fitter is based on the minimization of a global χ^2 value built from the hit location and estimated trajectory. The geometry of ATLAS and physical environment (magnetic field and density of material) is implemented to the fit methods as a weights of hits i.e. hits far from predicted trajectory are suppressed. For these purposes second order differential equations of motion has to be numerically calculated to predict the trajectory of particles traversing through various materials and magnetic field.

Especially for the muon spectrometer, there are two muon reconstruction softwares: MOORE and Muonboy Ref. [25]. The MOORE uses the hits selected by pattern recognition as a seed for the segment (tangents to the trajectory) reconstruction. The track in Muon Spectrometer is reconstructed from these segments. The Muonboy is based on propagating the regions of activity from chamber to chamber. In the first step, a cone of $\triangle\eta \times \triangle\phi = 0.4 \times 0.4$ is created around a hit on the RPC. In the second step, hits in MDT which are also included in the region of activity are found. In the third step,

the segments are created using the information (amount of caught charge) from drift tubes Fig. 8.2 that as in the previous case are used to the track reconstruction.

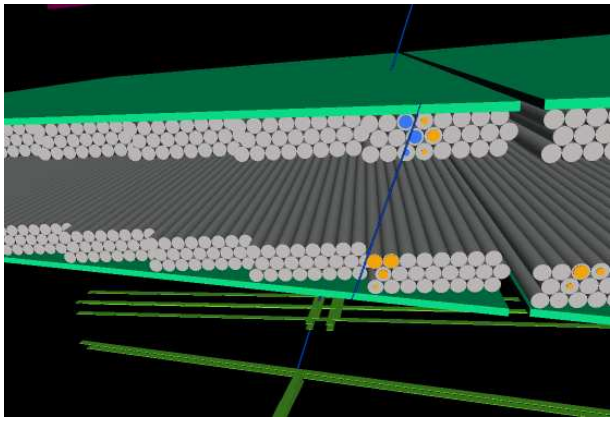

Figure 8.2: Drift tubes in muon spectrometer Ref. [21].

Although the track of muon can be reconstructed by both Inner detector and Muon Spectrometer independently, it can also be done from information of both detectors using outside-in extrapolation and some of the fit method. Such muons are called combined. In the case of so called standalone muons, the information is taken only from muon spectrometer. Third case are Tagged muons which are identified by Inner Detector and information about energy deposition in Calorimeter. These methods are used only in the offline reconstruction because it needs larger CPU time.

Chapter 9

Muons in TileCal, Data Analysis

As mentioned in previous chapters, the uniformity gives us a tool for monitoring and calibrating TileCal response. This chapter contains several interesting plots of uniformity and muon energy loss from data taken during pp collisions 2011. These plots are also compared to Monte Carlo data.

This chapter is divided into sections according to the physical quantities which have been plotted. The first two sections pay attention to the methods of data analysis. The third section includes uniformity in η direction (section 9.3), where all muons with the same η but generally different ϕ were integrated over and the appropriate mean value was put into the graph. This has been done analogically for uniformity in ϕ direction (section 9.4) where η was integrated over. Section 9.5 contains the plots of uniformity in both directions, it means that the mean value of energy loss per unit length was given from spatial angle $\Delta\phi \times \Delta\eta = 0.1 \times 0.1$. Studies of the energy loss dependence on the energy of muons is presented in the last section 9.6.

9.1 Muon selection

Several cuts have been done for the selection and the isolation of muons:

- energy loss in LAr in cone $\Delta R < 0.4$ is smaller than 3 GeV.
- sum of transversal momenta without a muon in cone $\Delta R < 0.4$ is smaller than 2 GeV.

- transverse invariant mass is larger than 40 GeV.
- missing E_T is larger than 25 GeV.
- true trigger decision for muon is made.

where ΔR is defined as $\sqrt{\Delta\phi^2 + \Delta\eta^2}$. Differences $\Delta\phi$ and $\Delta\eta$ are measured from muon track in this case. First two cuts are responsible for the muon isolation. There is a high probability of the presence of a neutrino correlated with a muon after second two cuts thus the muon should come from a decay $W \to \mu\nu$.

The transversal momentum after all these cuts is shown in Fig. 9.1. One can see that MC and collision data are in perfect correspondence that is good certification for these cuts. In the next analysis, one more cut for the transversal momentum is added $P_T > 20GeV$ to reduce the negligible tail on the left part in Fig. 9.1. Same cuts have been made by Zhili Weng in his analysis Ref. [27].

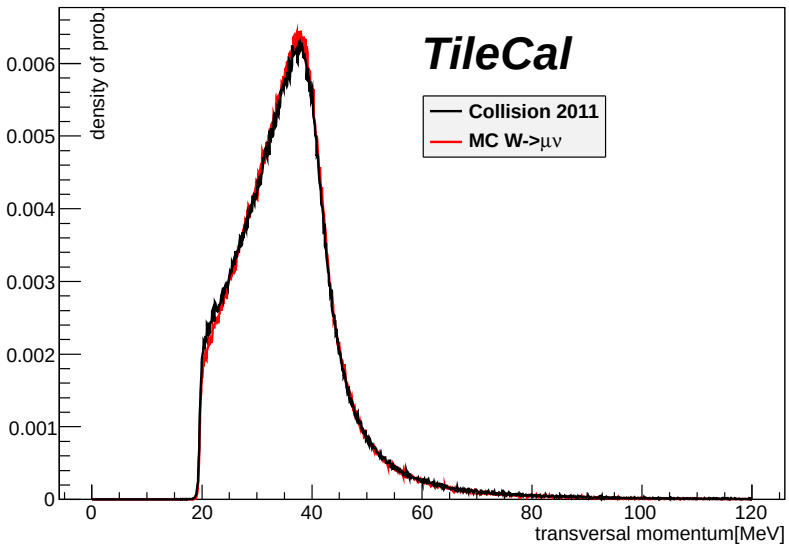

Figure 9.1: P_T spectrum of muons after selection criteria. MC is in good agreement with Collision data.

9.2 Determination of dE/dx

Energy loss per unit length is calculated as a fraction of energy loss summed over the cells in specific direction and path length of muon in the same direction. Only **cells along the path** of muon are included in the following analysis. The measurement can be influenced by pile-up in case that muon traverses only short length in some cell. Additional cut (deposited energy in one cell > 60 MeV) have been made to reduce this effect. Other possible methods of cell selection are discussed in Appendix B.

The response of many muons traversing TileCal in nearly the same direction (η, ϕ or both) is put into the histogram and 1% **truncated mean** is calculated. The upper 1% of events is cut away because there can be some undesirable particles which were not triggered out (for instance high energetic pions). Truncated mean and its influence on uniformity in η for all layers is shown in Fig. 9.2. Normal mean is shifted approximately about 0.25 MeV/cm upwards in comparison with truncated mean but the shape of uniformity is practically the same. The same shift can be found in Fig. 9.13.

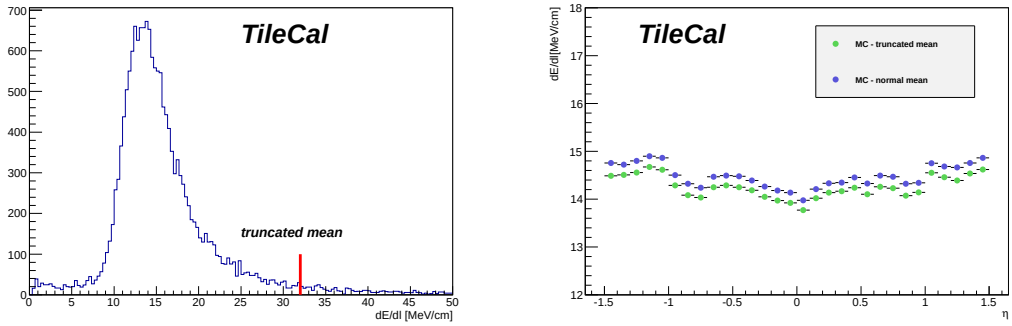

Figure 9.2: Left: example of a spectrum of energy loss per unit length for $\eta \sim 0.3$ and application of truncated mean. Right: its influence on total uniformity in η.

9.3 Uniformity in η

Plots of uniformity in η integrated over ϕ for each layer are shown in Fig. 9.3 (layer A), Fig. 9.4 (layer BC) and Fig. 9.5 (layer D).

Collision plots suits very well with MC data. Small peak in region $\eta \sim 0$ in Fig. 9.3 and Fig. 9.5 corresponds to perpendicular position of tiles to the beam i.e. the direction of muon motion is parallel with tiles. This peak is absent in Fig. 9.4 that can be caused by approximately two times longer path through layer BC than through layers A or D. More about this effect can be found in Appendix D.

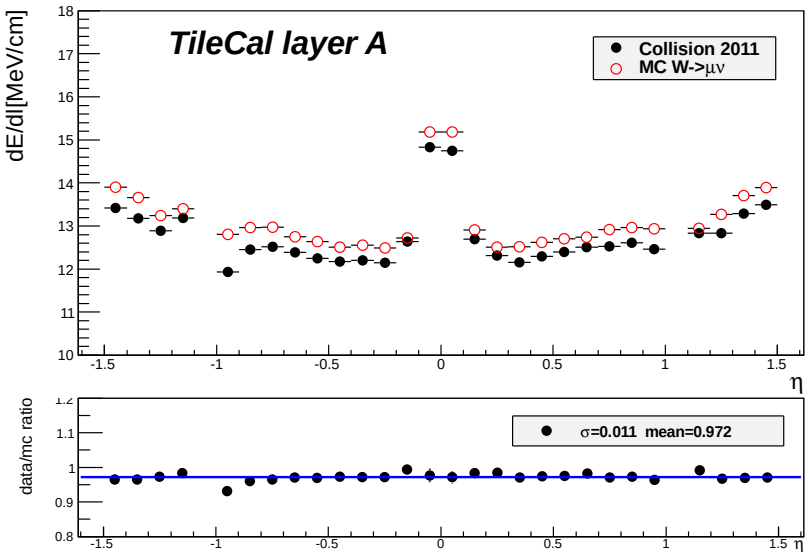

Figure 9.3: The uniformity in η integrated over ϕ for layer A and appropriate data/mc ratio calculated for both barrels. The mean and σ of data/mc is calculated for both barrels. Separate values for LB and EB of data/mc ratio can be found in table 9.2.

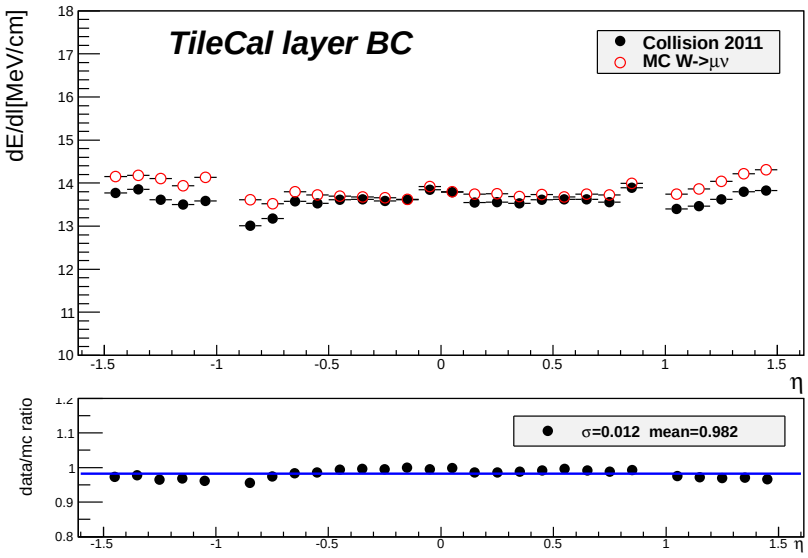

Figure 9.4: The uniformity in η integrated over ϕ for layer BC and appropriate values data/mc ratio. The mean and σ of data/mc is calculated for both barrels. Separate values for LB and EB of data/mc ratio can be found in table 9.2.

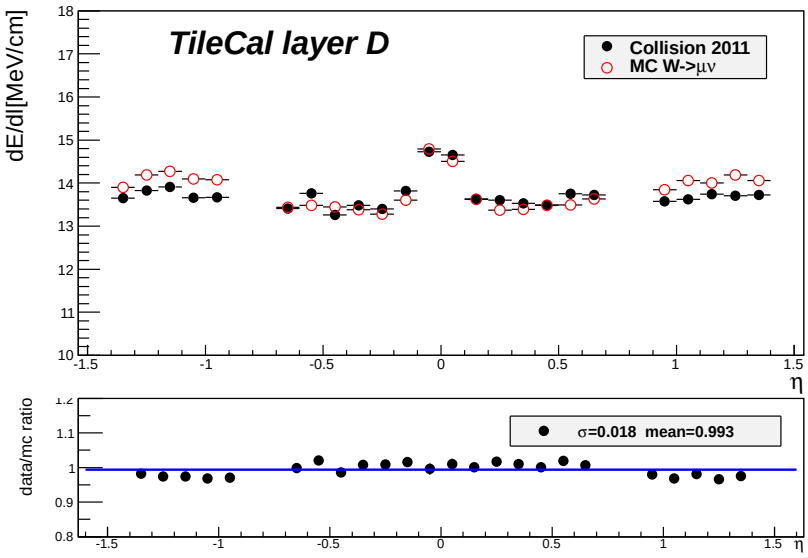

Figure 9.5: The uniformity in η integrated over ϕ for layer D. appropriate data/mc ratio calculated for both barrels. The mean and σ of data/mc is calculated for both barrels. Separate values for LB and EB of data/mc ratio can be found in table 9.2.

Comparison with other analysis

Values of mean and σ (standard deviation Ref. [28]) of data/mc ratio in Fig. 9.3, Fig. 9.4 and Fig. 9.5 includes both LB and EB. These quantities are evaluated separately for each layer in LB and each layer EB in table 9.2. Values in this table can be compared to the analysis of Zhili Weng in table 9.1. Same results can be derived from table 2 at Cosmic Analysis at TileCal Approved Plots Ref. [29].

One can expect value of the mean of data/mc ratio approximately 1. Deviation from 1 implies possible changes EM scale (see section 4.3) in ATLAS from EM scale set at Test Beam Ref. [17], Ref. [26]. Both analysis show that this deviation is less than 4% in all layers.

Fig. 9.3, Fig. 9.4 and Fig. 9.5 are also in good agreement with Fig. C.1 and Fig. C.2 in Appendix C. There is a little shift in comparison with these graphs. This is probably caused by another method of cell selection but important is that shapes of uniformities are basically the same as well as the

data/mc ratio. Note that error bars for dE/dx uncertainty are smaller than the size of marker in Fig. 9.3-9.5 and the same pays for almost all points in Fig. C.1 and Fig. C.2.

	data 2010/MC	**data 2011/MC**
LB-A	0.962±0.003	0.960±0.004
LB-BC	0.972±0.002	0.974±0.003
LB-D	1.007±0.003	1.010±0.004
EB-A	0.961±0.004	0.970±0.005
EB-B	0.975±0.003	0.979±0.004
EB-D	0.981±0.003	0.991±0.004

Table 9.1: Results of data/mc ratio calculated by Zhili Weng Ref. [27]. Notation: LB-A means Long Barrel layer A and analogically for other layers and barrels.

	data 2011/MC
LB-A	0.972±0.011
LB-BC	0.989±0.010
LB-D	1.007±0.015
EB-A	0.973±0.009
EB-B	0.970±0.003
EB-D	0.974±0.004

Table 9.2: Results of data/mc ratio calculated in this work. Notation: LB-A means Long Barrel layer A and analogically for other layers and barrels.

9.4 Uniformity in ϕ

Plots of uniformity in ϕ integrated over η are in Fig. 9.6 (layer A), Fig. 9.7 (layer BC) and Fig. 9.8 (layer D). One can see that TileCal is much more uniform in ϕ than in η.

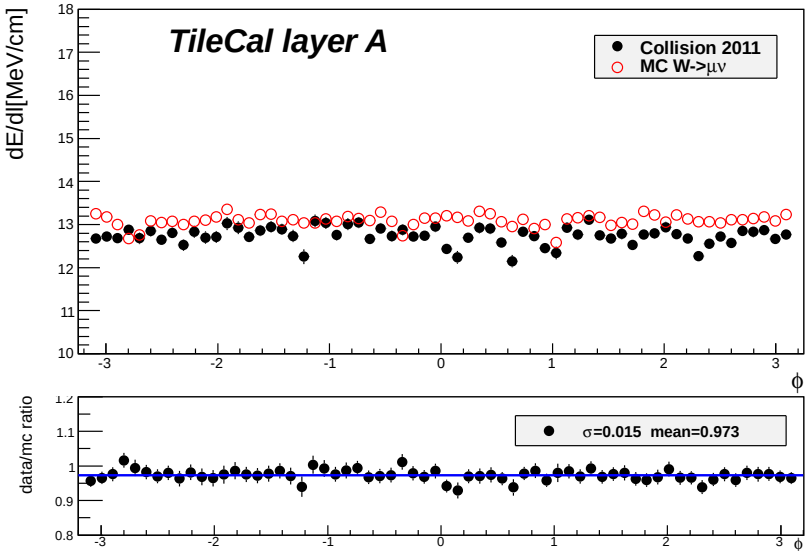

Figure 9.6: The uniformity in ϕ integrated over η for layer A and appropriate data/mc ratio.

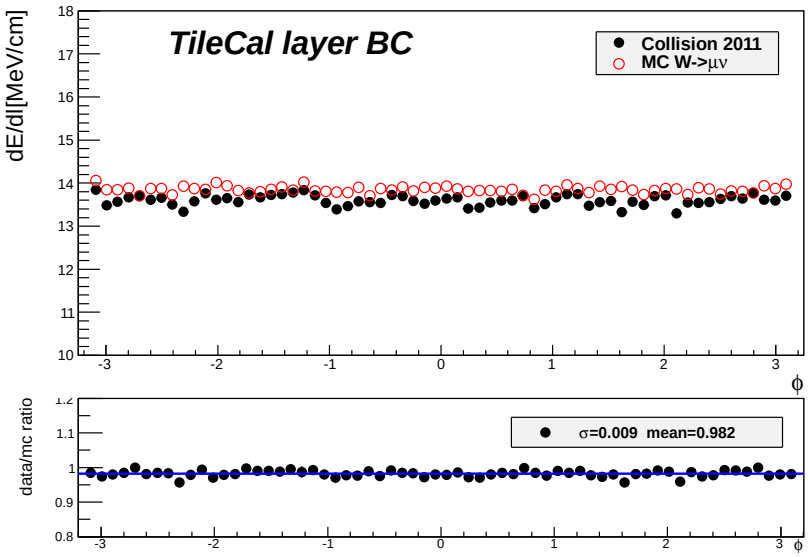

Figure 9.7: The uniformity in ϕ integrated over η for layer BC and appropriate data/mc ratio.

Comparison to other analysis

One can find plots of uniformity in ϕ at pages of TileCal Public Results Ref. [29] but they did not provide any values to compare. However, we can compare plots in Fig. 9.6, Fig. 9.7 and Fig. 9.8 with plots of Zhili Weng Fig. C.3 and Fig. C.4 in Appendix C. We can also compare mean values of data/mc ratio and appropriate σ including both LB and EB in Fig. 9.6, Fig. 9.7 and Fig. 9.8 to the same values in Fig. 9.3, Fig. 9.4 and Fig. 9.5. These values should be nearly the same as it is monitoring the same layer. For layer A, it is 0.972±0.011 for uniformity in η and 0.973±0.015 in ϕ. Same quantities for layer BC are 0.982±0.012 in η and 0.982±0.009 in ϕ. There is also good agreement for layer D: 0.993±0.018 in η and 0.995±0.014 in ϕ.

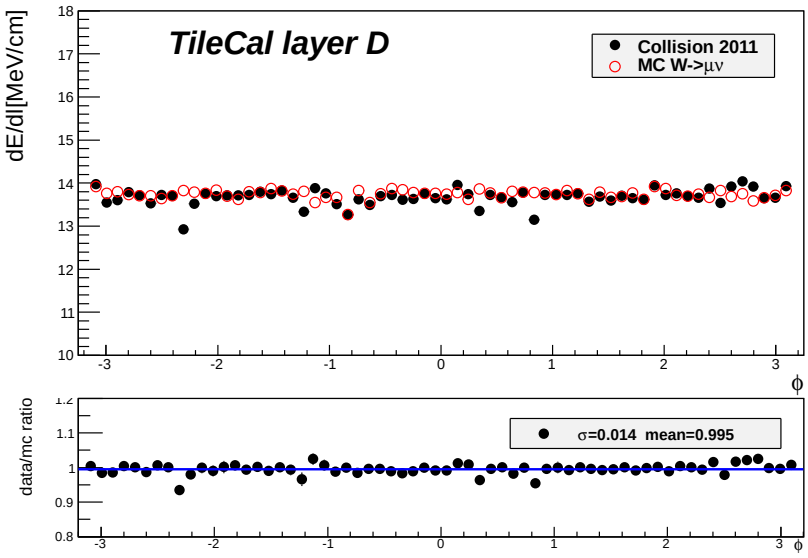

Figure 9.8: The uniformity in ϕ integrated over η for layer D and appropriate data/mc ratio.

9.5 Uniformity in η and ϕ

There are 6 plots of uniformity and occupancy in both direction for Monte Carlo data in Fig. 9.9 and six plots for Collision data in Fig. 9.10. These graphs are not so precise as the statistics is smaller then in previous sections (sections 9.3, 9.4) when one of angle was integrated over. But it gives a tool for spatial monitoring of whole TileCal.

Dead cells or cells with bad response are masked and the signal is not read from them. There is more masked cells (blue or white lines in occupancies) in the Collision data than in Monte Carlo. That can be also compared with masked cells in the end of 2011 Fig. 9.11. There are some missing masked cells in Fig. 9.10 in comparison with Fig. 9.11 reflecting the changes of TileCal status during the year 2011 (There is more masked cells in the end of 2011). Occupancies in Fig. 9.10 has more masked or bad cells on the left side ($\eta < 0$) that leads to a little asymmetric state of TileCal.

Long red sectors in uniformities and long blue sectors in occupancies corresponds to gaps which were cut away in plots in previous sections. There are also visible violet parts in layer A which correspond to the structure of

muon spectrometer, see Fig. 9.12. We have low number of muons in these directions thus appropriate low response does not influence the results a lot. [1]

[1] The information from muon spectrometer is needed for precise reconstruction of muon (chapter 8) so we have low number of muons in dead directions of muon spectrometer.

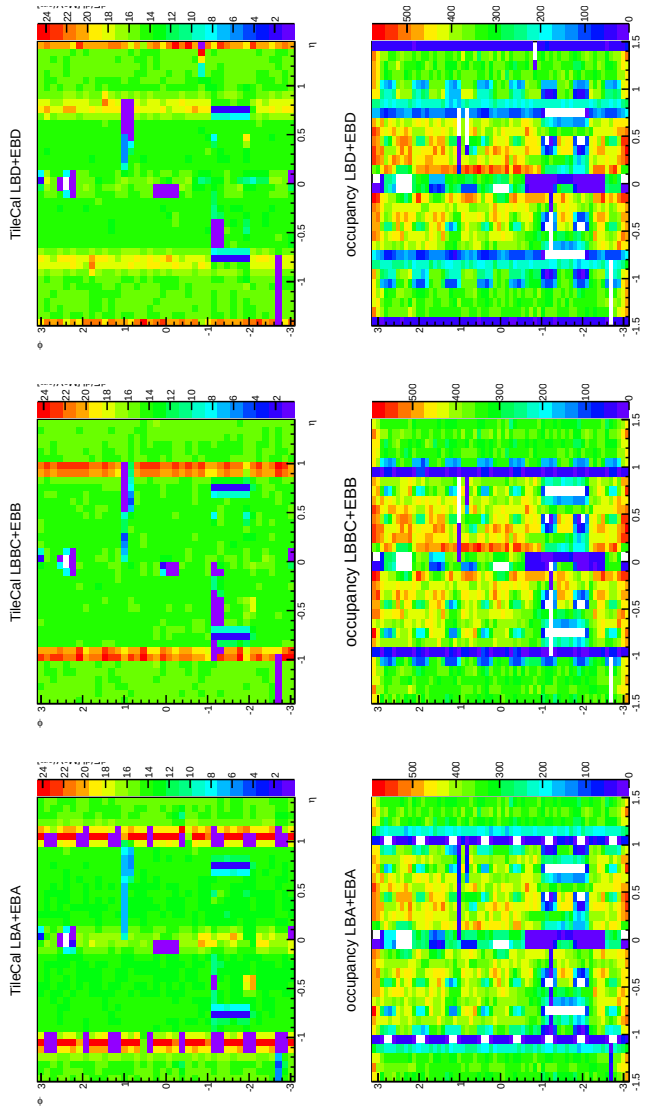

Figure 9.9: The monitoring in both ϕ (vetical axis) and η (horizontal axis), MONTE CARLO data. Colour represents dE/dx [MeV/cm] in upper figures of uiformity. Occupancies: blue-white vertical (ϕ =const.) parts corresponds to masked cells, blue-white long horizontal parts (η =const.) are caused by gap, blue-violet parts in LB correspond to the structure of muon spectrometer. Uniformities: light blue or violet vertical parts corresponds to masked cells.

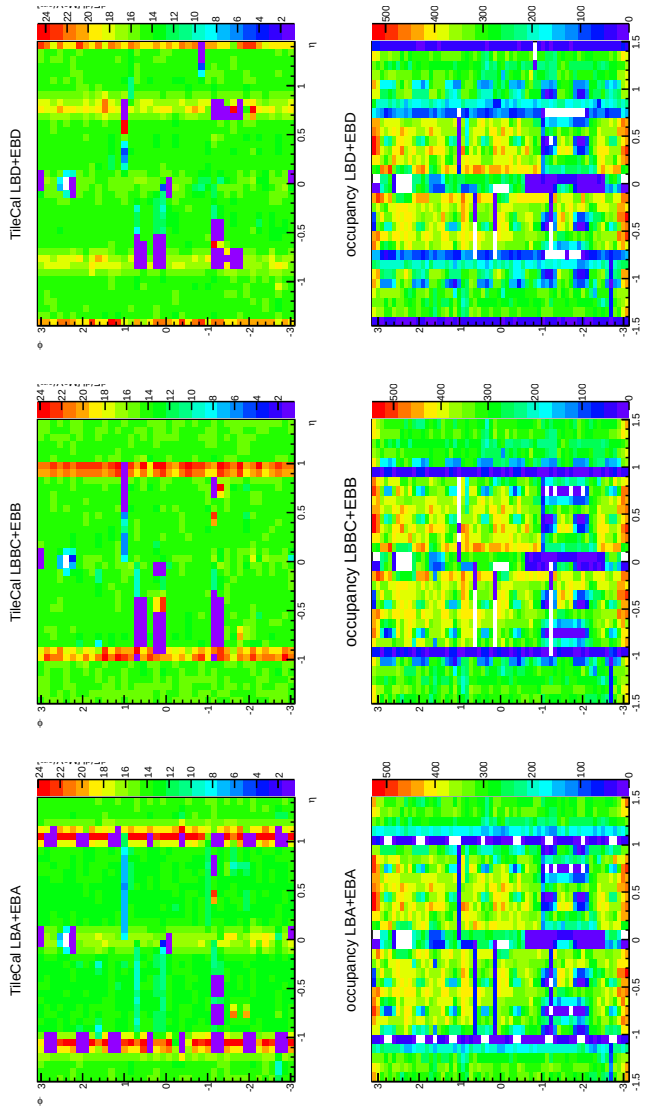

Figure 9.10: The monitoring in both ϕ (vertical axis) and η (horizontal axis). Colour represents dE/dx [MeV/cm] in upper figures of uniformity. COLLISION data. Occupancies: blue-white vertical (ϕ =const.) parts corresponds to masked cells, blue-white long horizontal parts (η =const.) are caused by gap, blue-violet parts in LB correspond to the structure of muon spectrometer. Uniformities: light blue or violet vertical parts corresponds to masked cells.

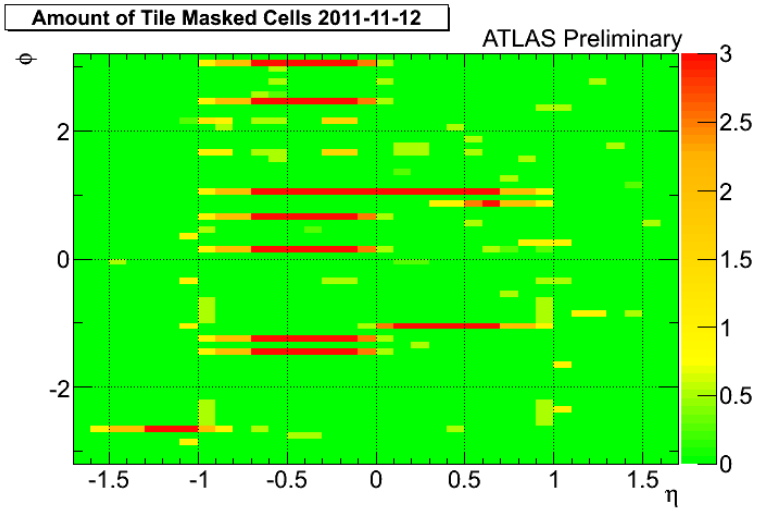

Figure 9.11: Masked Cells 2011 [29].

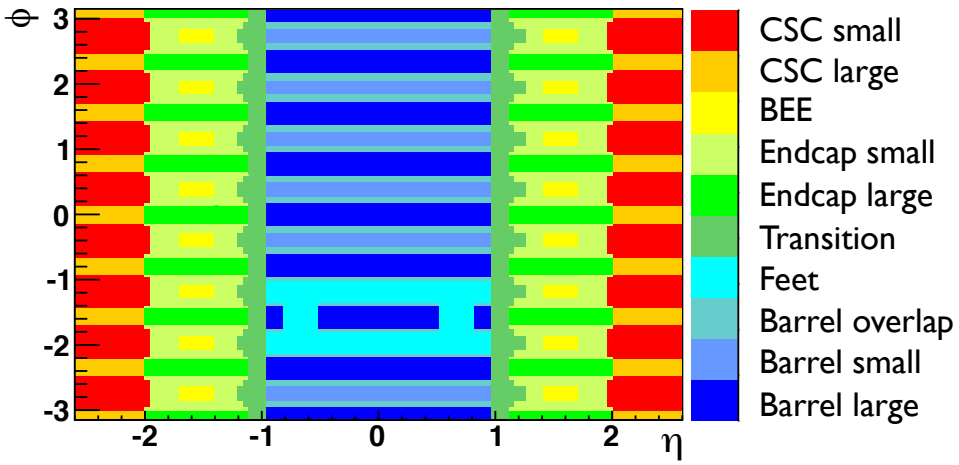

Figure 9.12: Structure of the Muon Spectrometer [30].

9.6 Muon energy loss, dependence on energy

Muon energy loss in whole TileCal increases with the energy as it is shown in Fig. 9.13. Blue dashed line corresponds to the ionization i.e. Bethe-Bloch Eq. (7.1). Four blue squares represent the results given from test beam on

TileCal prototype[1] Ref. [18]. MC studies (red points) are in good agreement with collision data (black points). Blue empty circles correspond to the MC studies but energy loss is calculated as a normal mean (not as a truncated mean as in the rest of the work). One can see that truncated mean does not have impact on steepness.

When energy of muon exceeds 100 GeV, the dependence grows up a little bit faster then Bethe-Bloch predication. It can be explained by radiation loss of muons.

Important note is that e/μ factor (electron to muon energy conversion factor, more information can be found for example in Ref. [18]) does not influence a steepness of energy loss dependence on muon energy because this factor has approximately constant value 0.91 (subtly dependent on the method of determeination of dE/dx) in the range of energies 20-150 GeV Ref. [18].

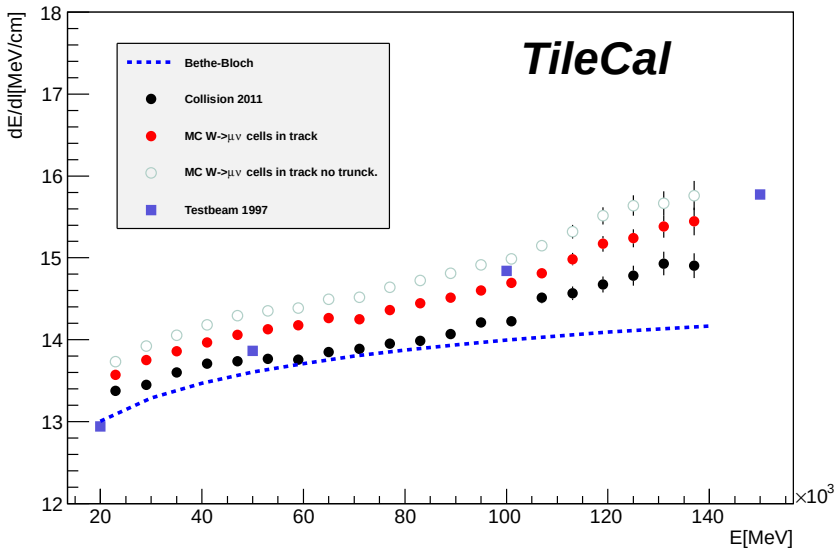

Figure 9.13: Energy loss of muon per unit length, dependency on energy. Comparison of Collision data, MC, Behte-Bloch formula and Test-beam is depicted by different marker or line style.

[1]Tests on TileCal prototype 1995-1997 used a copy of TileCal module with sligthly different dimensions. Instead of 152 cm in radial direction it had 180 cm. Studies for dE/dx dependency on energy of muons have been done for $\eta \sim 0.18$.

Chapter 10

Summary and conclusion

The response of Tile calorimeter to muons was investigated in present work. The uniformity in η and ϕ, a tool for monitoring TileCal, was plotted to the graphs. Analysis of collision data 2011 were compared to the results of MC using data/mc ratio. This ratio varies from 1 maximally by 4% for all layers that was also estimated by other analysis. A higher response in region of $\eta \sim 0$ was observed and brief explanation of this effect was given.

We have also tried to investigate the dependence of muon energy loss on its energy in range 20-140 GeV. Good agreement with MC and results from test beam [18] was observed. The influence of radiative losses was observed as a deflection from Bethe-Bloch formula at energies higher than 100 GeV.

Appendix A

Cell positions and dimensions

Precise calculation of muon track length through TileCal is needed to determine dE/dl. Values in following tables were used for these purposes. Values of positions and dimensions are introduced in millimeters.
Notation: R ≡ radial position of the cell centre, ΔR ≡ radial dimension of the cell, Z ≡ z-position of the cell, ΔZ ≡ dimension of the cell in z direction, LB-A ≡ long barrel layer A and analogically for other layers.

LB-A	**A1**	**A2**	**A3**	**A4**	**A5**	**A6**	**A7**	**A8**	**A9**	**A10**
Z	123.24	369.72	620.76	876.37	1141.10	1419.53	1707.09	2012.90	2341.54	2656.48
ΔZ	246.48	246.48	255.61	255.61	273.86	282.99	292.12	319.51	337.77	292.12
R	2450.0	2450.0	2450.0	2450.0	2450.0	2450.0	2450.0	2450.0	2450.0	2450.0
ΔR	300.0	300.0	300.0	300.0	300.0	300.0	300.0	300.0	300.0	300.0

LB-BC	**BC1**	**BC2**	**BC3**	**BC4**	**BC5**	**BC6**	**BC7**	**BC8**	**B9**
Z	151.06	454.70	762.89	1078.71	1405.33	1746.02	2104.18	2483.40	2642.79
ΔZ	-	-	-	-	-	-	-	-	319.51
R	3020.0	3020.0	3020.0	3020.0	3020.0	3020.0	3020.0	3020.0	2795.0
ΔR	840.0	840.0	840.0	840.0	840.0	840.0	840.0	840.0	390.0

Important note: *Values of Z position of cells for the right EB ($\eta > 0$) has to be increased by 10 mm*

LB-D	**D0**	**D1**	**D2**	**D3**
Z	0.0	734.87	1497.12	2346.10
ΔZ	730.30	739.44	785.08	912.88
R	3630.0	3630.0	3630.0	3630.0
ΔR	380.0	380.0	380.0	380.0

	D4	**C10**
Z	3395.0	3501.85
ΔZ	309.0	94.70
R	3630.0	3215.0
ΔR	380.0	450.0

EB-A	**A12**	**A13**	**A14**	**A15**	**A16**
Z	3646.64	3956.95	4440.67	4970.025	5681.91
ΔZ	164.28	456.339294	511.10	547.61	876.17
R	2450.0	2450.0	2450.0	2450.0	2450.0
ΔR	300.0	300.0	300.0	300.0	300.0

EB-B	**B11**	**B12**	**B13**	**B14**	**B15**
Z	3710.53	4102.98	4623.21	5189.07	5800.56
ΔZ	292.06	492.85	547.61	584.11	638.88
R	2870.0	2870.0	2870.0	2870.0	2870.0
ΔR	540.00	540.00	540.00	540.00	540.00

EB-D	**D5**	**D6**
Z	4157.74	5435.49
ΔZ	1186.48	1369.018
R	3480.0	3480.0
ΔR	680.0	680.0

Appendix B

Cell selection

There are several ways how to choose the cells that contribute to the energy loss of the muon. Three of them are compared in plots of total uniformity (total stands for whole TileCal, not only for layers as in previous sections) Fig. B.1 for Collision data and Fig. B.2 for MC. Gray colour corresponds to the case when all cells in cone $\Delta R < 0.4$ have been included to the total energy loss in TileCal and muon path length is calculated as a total path length in TileCal in appropriate direction, see Fig. 7.2. Brown colour corresponds to the case when only cells which are situated along the track of muon and have response larger than 60 MeV are included. Green colour corresponds to a method which takes exactly the same cells as in previous case to calculate energy loss but muon path length is given only from that cells (path length calculated that way can be generally shorter than total muon path length in TileCal). For example if any cell is in the track but its response is lower than 60 MeV, than the length passed through this cell is not included to the whole track. For our analysis only **brown method** is chosen.

In can be a little bit surprising that there is no peak at $\eta \sim 0$ for brown method as in Fig. 9.3 and Fig. 9.5. As was mentioned in section 9.3 this efect is missing in layer BC because of longer path length in this layer (more than 80 cm) and thus lower sample fraction variation Ref. [31]. The same pays when the path length is calculated for whole TileCal (more than 152 cm in $\eta \sim 0$).

One can see a little asymmetry in case of Collision data Fig. B.2 in $\eta \sim -0.9$. Fig. 9.3 (layer A) and Fig. 9.4 (layer BC) also partially reveal this asymmetry. It can be caused by higher number of cells with response

lower than 60 Mev in this direction. Path length in such cells is included to the total path length but response of such cells is not. This hypothesis is supported by the fact that the green method in Fig. B.2 is more symmetrical.

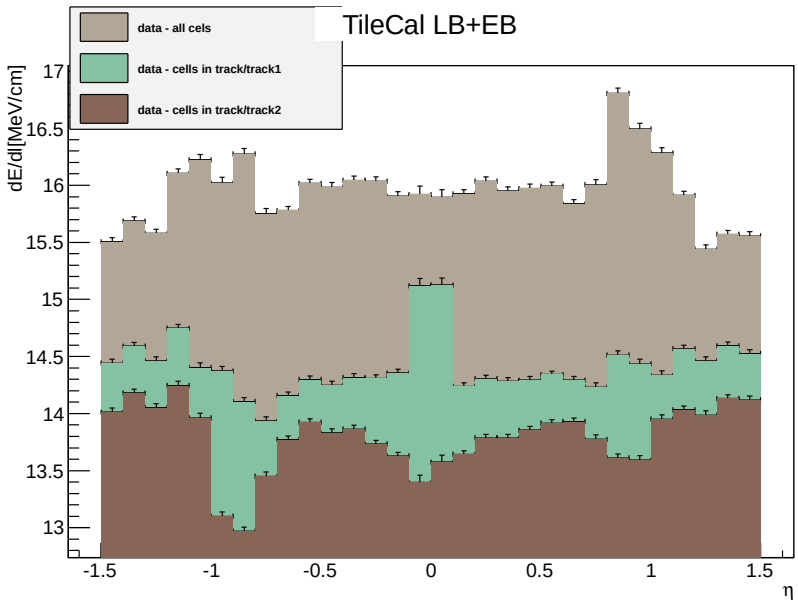

Figure B.1: Collision data: The uniformity in η integrated over ϕ, all layers. Notation: track1 means that muon path was calculated and added only in cells, which had response higher than 60 MeV, track2 means that muon path was calculated in all cells along the path of muon even if they did not respond at all (it is equivalent to total path length of muon in TileCal).

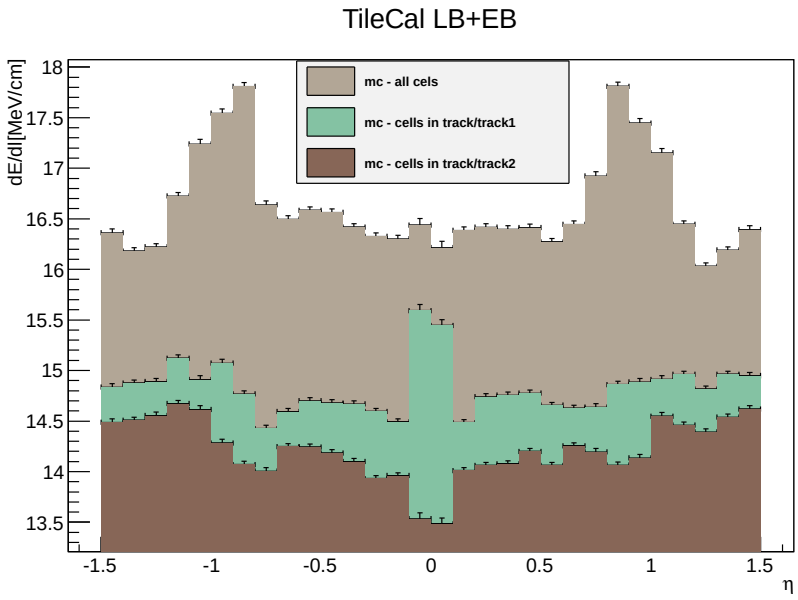

Figure B.2: Monte Carlo: The uniformity in η integrated over ϕ, all layers. Notation: track1 means that muon path was calculated and added only in cells, which had response higher than 60 MeV, track2 means that muon path was calculated in all cells along the path of muon even if they did not respond at all.

Appendix C

Other analysis of TileCal uniformity

There are three plots of uniformity in η in Fig. C.1 and Fig. C.2 and three plots of uniformity in ϕ in Fig. C.3 and Fig. C.4. All these plots are provided by Zhili Weng Ref. [27]. In comparison with our results Fig. 9.3-9.8 there is a little bit higher average response, approximately 15 MeV/cm, that is caused by another method of cell selection.

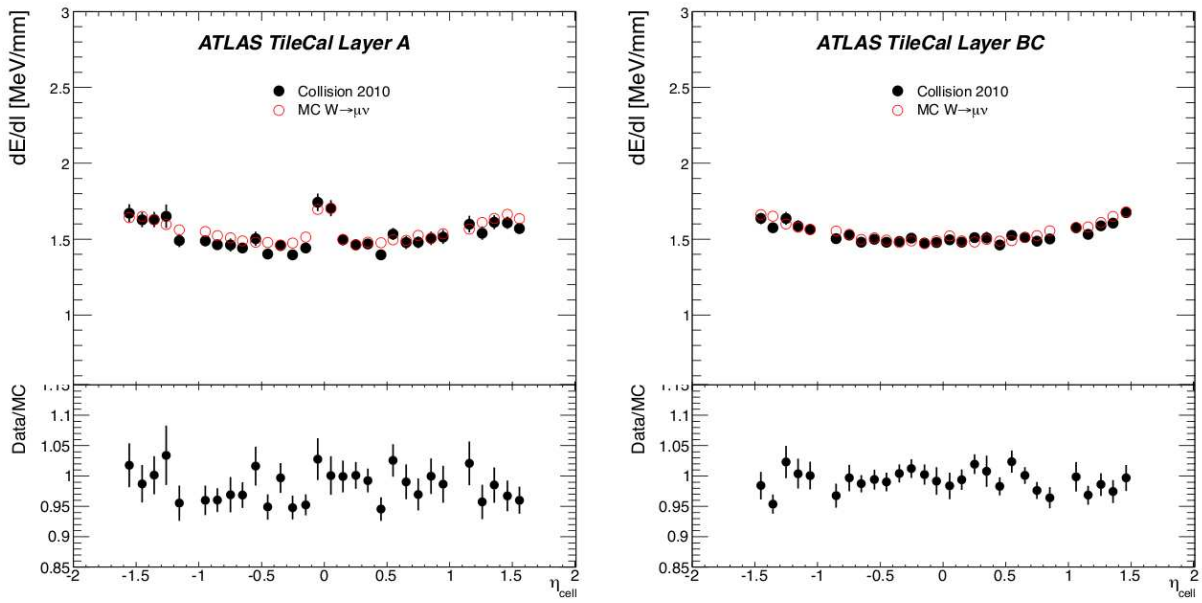

Figure C.1: Uniformities in η plotted by Zhili Weng Ref. [27].

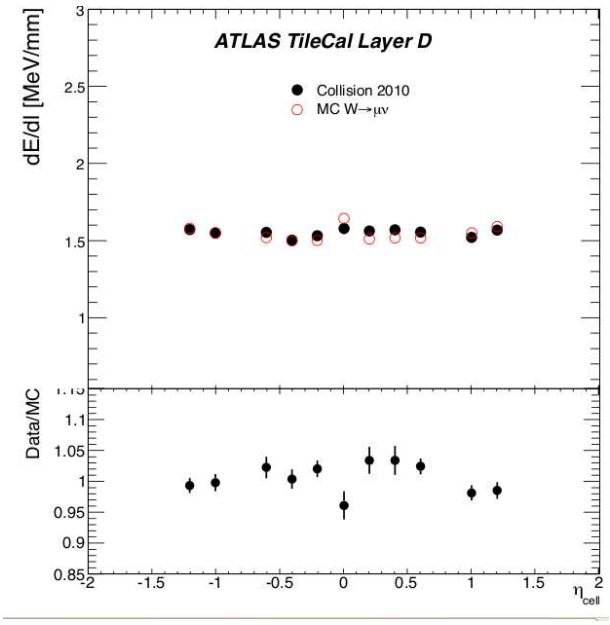

Figure C.2: Uniformity in η plotted by Zhili Weng Ref. [27].

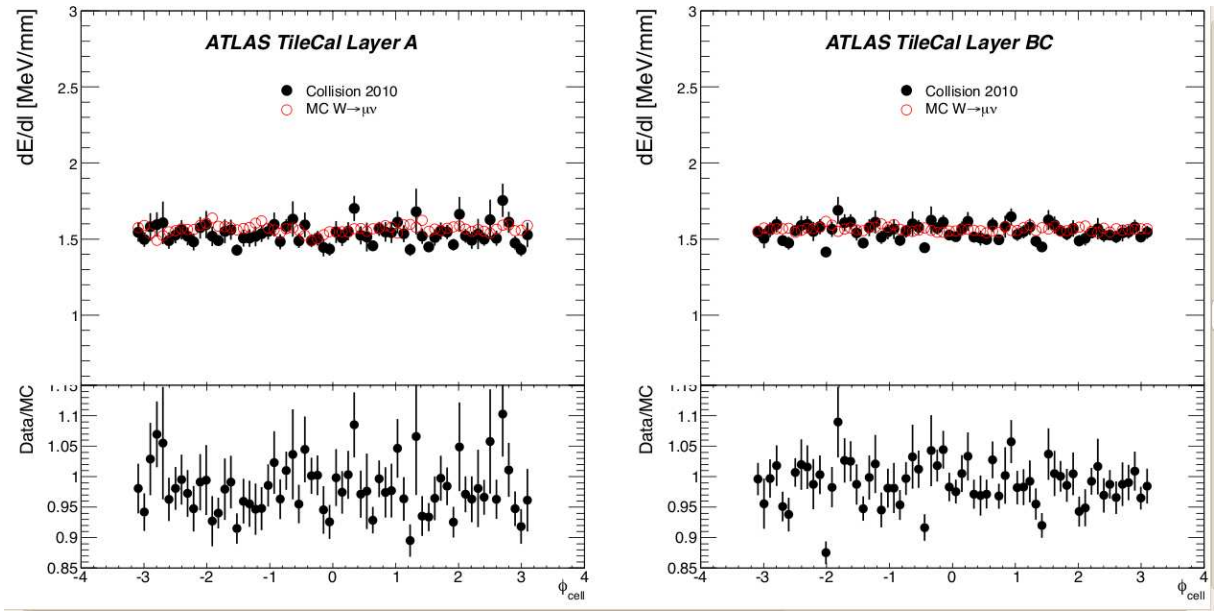

Figure C.3: Uniformities in ϕ plotted by Zhili Weng Ref. [27].

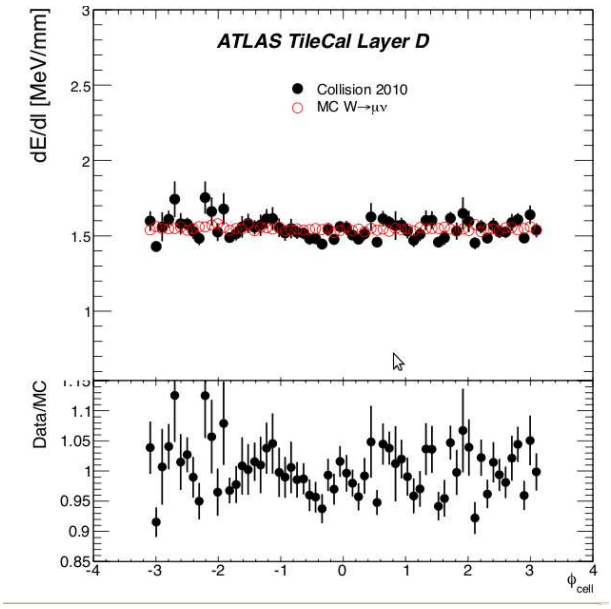

Figure C.4: Uniformity in ϕ plotted by Zhili Weng Ref. [27].

Appendix D

Problem at $\eta \sim 0$

As it was mentioned in section 9.3 there is little bit higher response in direction $\eta \sim 0$, see Fig. 9.3, Fig. 9.5. That is caused by nearly parallel direction of muon path with position of tiles. Thus the ratio of path in iron and path in scintillator varies extensively in this direction. This variation is much lower in case of higher pseudorapidity $\eta > 0.15$ Ref. [31]. This has effect on sampling fraction defined as fraction of energy loss in scintillator and energy loss in both iron and scintillator. Sampling fraction then influence the e/μ factor and therefore also value of measured deposited energy. Muons which traverse longer path in scintillator has higher response. Detailed studies of the response in direction $\eta \sim 0$ is shown in Fig. D.1.

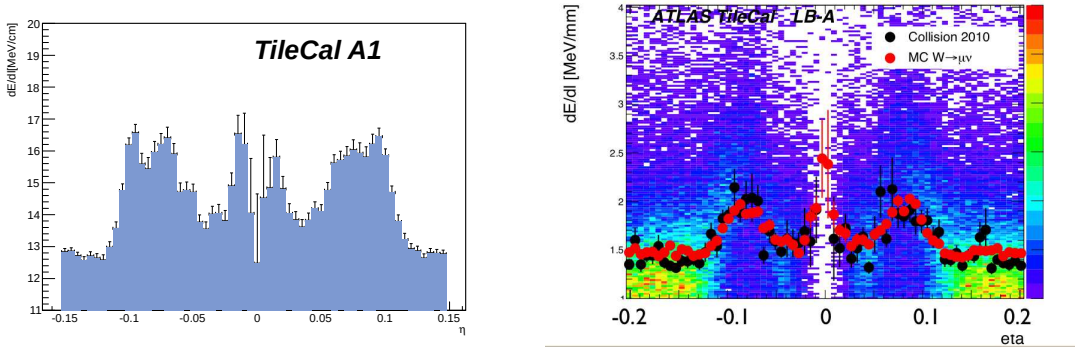

Figure D.1: Detailed study of uniformity at $\eta \sim 0$ provided by Zhili Weng right Ref. [27]. Red points in the right figure corresponds to the bin attitudes in the left figure of MC studies of the present work. One can see in the right figure that the effect of higher response at this direction is well reproduced by MC. There are four peaks: two at $\eta \sim \pm 0.02$ and two broader peaks at $\eta \sim \pm 0.07$ where response of cells is higher, approximately 16 MeV/cm. This effect causes the peak in $\eta < 0.01$ region in Fig. 9.3. Red points in the right figure are a little bit higher (approximately 15 Mev/cm at $\eta = 0.15$) because another method of cell selection.

Bibliography

[1] CERN public web:
`http://public.web.cern.ch/public/en/research/AccelComplex-en.html`

[2] ATLAS collaboration: *The ATLAS Experiment at the CERN Large Hadron Collider*, JINST 3 S08003, 2008

[3] N. C. Benekos, G. Dedes, D. Rebuzzi, and M. Schott: *Atlas muon spectrometer simulation and its validation algorithms*, CERN, Geneva, Tech. Rep. ATL-COM-MUON-2007-003, Mar 2007.

[4] A. R. Martinez: *Studies with Muons in Atlas: TileCal Level-2 Trigger and MSSM Higgs Discovery Reach*, Valencia, 2009

[5] ATLAS collaboration: *Readiness of the ATLAS Tile Calorimeter for LHC collisions*, Eur. Phys. J. C (2010) 70: 1193–1236

[6] C. Amsler and M. Doser: *Review of Particle Physics*,Phys.Lett. B 667, 2008

[7] C. Bohm et al.: *ATLAS Tilecal Digitizer Test System and Quality Control*, CERN-ATL-COM-TILECAL-2004-008, CERN, Geneva, 2004

[8] L. Pribyl: *The Calibration of a Hadron Calorimeter TileCal for the ATLAS Experiment at the LHC Accelerator*,Prague, 2003

[9] Valencia TileCal homepage: `http://ific.uv.es/tical/old/rod/index.html`

[10] M. Pagacova: *Time resolution of TileCal and searches for heavy metastable praticles*

[11] C. Solans: *Performance of the ATLAS Hadronic Tile Calorimeter at the LHC Startup*, ATL-TILECAL-PROC-2009-003

[12] W. Lohman, R. Kopp, R. Voss: *Energy loss of muons in the energy range 1-10 000 GeV*, CERN 85-03, 1985

[13] J. Carvalho: *The TileCal/ATLAS calorimeter calibration systems*, ATL-TILECAL-PROC-2011-011

[14] http://root.cern.ch/root/doc/RootDoc.html

[15] J. Schovancova: *Atlas distributed computing*, ATL-SOFT-SLIDE-2011-093. Geneva CERN, 2011

[16] Atlas public web: `http://www.atlas.ch/trigger.html`

[17] P. Adragan et al.: *Testbeam studies of production modules of the ATLAS Tile Calorimeter* , ATL-TILECAL-PUB-2009-002

[18] Ziad. J. Ajaltouni et al.: *Response of the ATLAS tile calorimeter prototype to muons*, CERN-PPE-96-173

[19] Technical design report: `http://atlas.web.cern.ch/Atlas/GROUPS/PHYSICS/TDR/access.html`

[20] `http://www.atlas.ch/news/2011/status-report-dec-2011.html`

[21] `http://atlas-service-enews.web.cern.ch/atlas-service-enews/2007-8/features_07-8/features_vp1-3.php`

[22] Z. van Kesteren: *Identification of muons in Atlas*

[23] R. Fruehwirth et al.: *Applications of kalman filtering to track and vertex fitting*, Nucl. Inst. Meth. A 262, 1987.

[24] T. Cornelissen et al.: *The global χ^2 track fitter in atlas*, Jour. of Phys., conference series 119 (2008) 032013, 2008.

[25] R. Nicolaidou, L. Chevalier, S. Hassani, J.F. Laporte, E. Le Menedeu, A. Ouraou: *Muon identification procedure for the ATLAS detector at the LHC using Muonboy reconstruction package and tests of its performance using cosmic rays and single beam data*, IOP Publishing, CHEP09, 2010

[26] A. Dotti, C. Santoni, G. Usai, Z. Weng: *Calibration of the ATLAS hadronic barrel calorimeter TileCal using 2008, 2009 and 2010 cosmic rays data*, ATL-TILECAL-PUB-2011-001

[27] Presentation of Z.Weng:
`https://indico.cern.ch/conferenceDisplay.py?confId=141276`

[28] `http://en.wikipedia.org/wiki/Standard_deviation`

[29] TileCal public plots:
`https://twiki.cern.ch/twiki/bin/view/AtlasPublic/ApprovedPlotsTile`

[30] `https://atlas.web.cern.ch/Atlas/GROUPS/PHYSICS`
`/CONFNOTES/ATLAS-CONF-2011-063/`

[31] Yu A. Budagov et al.: *Study of TileCal Sampling Fraction for Improvement of Monte-Carlo Data Reconstruction*, ATL-TILECAL-PUB-2006-006